

Imaging nonequilibrium atomic vibrations with x-ray diffuse scattering

M. Trigo^{*,*}, J. Chen, and V. H. Vishwanath

PULSE Institute, SLAC National Accelerator Laboratory, Menlo Park, CA 94025, USA

Y. M. Sheu[†]

*FOCUS Center and Department of Physics,
University of Michigan, Ann Arbor, MI 48109, USA*

T. Graber and R. Henning

*The Center for Advanced Radiation Sources,
University of Chicago, Chicago IL 60637, USA*

D. A. Reis

*PULSE Institute, SLAC National Accelerator Laboratory, Menlo Park, CA 94025, USA and
Department of Photon Science and Applied Physics,
Stanford University, Stanford, CA 94305, USA*

(Dated: October 25, 2010)

Abstract

We use picosecond x-ray diffuse scattering to image the nonequilibrium vibrations of the lattice following ultrafast laser excitation. We present images of nonequilibrium phonons in InP and InSb throughout the Brillouin-zone which remain out of equilibrium up to nanoseconds. The results are analyzed using a Born model that helps identify the phonon branches contributing to the observed features in the time-resolved diffuse scattering. In InP this analysis shows a delayed increase in the transverse acoustic (TA) phonon population along high-symmetry directions accompanied by a decrease in the longitudinal acoustic (LA) phonons. In InSb the increase in TA phonon population is less directional.

I. INTRODUCTION

The interaction of hot carriers and phonons in solids is a fundamental problem with important technological implications. In polar semiconductors, a bottleneck in the decay of certain phonon-modes leads to increased electron scattering from the nonthermal phonons having a direct effect on carrier mobility and heat removal in devices¹. Detailed knowledge of the nonthermal phonon distribution has been limited by the lack of probes with sufficient temporal and momentum resolution. In this work we present the first picosecond images of nonequilibrium phonons throughout the Brillouin-zone in photoexcited semiconductors using time-resolved x-ray diffuse scattering. We find that the lattice remains significantly out of equilibrium with the delayed emission of transverse acoustic phonons up to a nanosecond after laser excitation, even though typical phonon lifetimes are only a few picoseconds². The results have broader implications for the detailed understanding of dynamical properties of materials where specific phonons in the Brillouin-zone play a defining role.

X-ray scattering is sensitive to short wavelength phonons, which reduce the intensity of Bragg peaks as well as produce structure in the diffuse scattering background^{3,4}. Prior x-ray experiments on nonequilibrium phonons were limited by time-resolution^{5,6} or to studying relatively long wavelength excitations⁷⁻⁹. Analysis of the equilibrium thermal diffuse scattering (TDS) had been used to determine interatomic force constants and phonon dispersion in relatively simple cases¹⁰⁻¹³ before inelastic neutron scattering became the preferred technique to study lattice dynamics¹⁴. With the advent of intense synchrotron x-ray sources, there was a renewed interest in TDS for measuring phonon dispersion¹⁵. In the current study, we exploit the relatively short x-ray pulses from these sources to measure nonequilibrium phonon dynamics in the time domain.

II. EXPERIMENTAL DETAILS

Experiments were performed at the BioCARS beamline of the Advanced Photon Source (APS) at Argonne National Laboratory. The samples were (001)-cut single crystals of InP and InSb. Photoexcitation of carriers was achieved using ~ 1 ps visible pulses from an optical parametric amplifier synchronized to the x-rays from the APS. The laser pulse energy at the sample was $\sim 62 \mu\text{J}$ focused to a 0.14×2.1 mm spot, well below the melting threshold

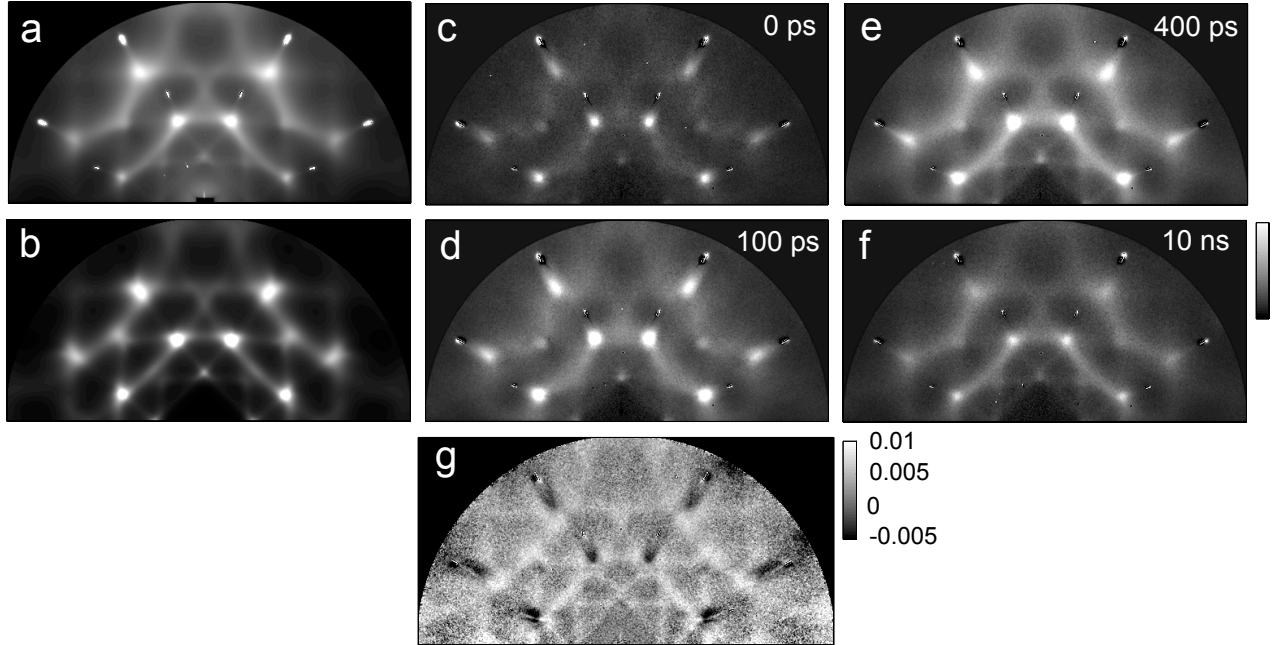


FIG. 1: (a) room temperature TDS image of InP at 15 keV oriented with (100) nearly parallel to the x-ray direction. (b) Calculated TDS from a Born model with six nearest-neighbors forces at 15 keV convolved with a 2 % Gaussian energy spread. (c) - (f) differences between laser-exposed and laser-off frames at delays $\Delta t = 0, 100, 400$ ps, and 10 ns, respectively (same scale). (g) Difference between frames at 400 ps and 100 ps normalized by the dark image, i.e. $[I(400 \text{ ps}) - I(100 \text{ ps})]/I(\text{off})$.

for InP and InSb and both recover fully between pulses at 40 Hz. The wavelength was set to 640 nm for InP and 700 nm for InSb. Similar results were obtained for InP at 640 nm and 700 nm. A dual undulator setup provided an x-ray photon flux at the sample of $\sim 10^{10}$ photons/pulse with photon energies in the range 12 – 15 keV in a < 4 % bandwidth. Single 100 ps x-ray pulses were isolated by a high-speed chopper at a rate of 40 Hz. The crystals were oriented at grazing incidence so that the x-rays were incident primarily along (100). Typical incidence angles of $\alpha = 0.3^\circ$ were used to match the volume probed by the x-rays with the laser excitation. A large area detector (MarCCD 165 mm diameter) placed 64 mm behind the sample collected the x-rays with scattering angles of up to $2\theta \sim 51^\circ$. In choosing the x-ray energy and crystal orientation, special care was taken to avoid Bragg reflections on the detector.

III. RESULTS AND DISCUSSIONS

Figure 1 (a) shows a static baseline (without laser excitation) x-ray scattering pattern from InP at room temperature taken with 15 keV x-ray energy. The upper half of the image is shown, the lower half being blocked by the sample. The detector captures a large solid angle of the Ewald sphere projected onto a plane. The intensity pattern originates primarily from (inelastic) scattering from thermally activated phonons and shows structure that reflects the details of the phonon dispersion in the material and the phonon population¹⁶. Figure 1 (b) shows the calculated image using a Born model for the interatomic forces, which captures the main observed features.

Ultrafast laser excitation initially produces a non-equilibrium state where phonons may not be populated according to the Bose factor. The evolution of this phonon population is encoded in the time-resolved diffuse scattering at different delays. As a function of laser-x-ray delay, t_i , we record a frame with laser exposure, $I(t_j)$, and a dark frame, $I(\text{off})$. In this manner we can subtract the initial room temperature diffuse scattering as well as any time-independent background. Figures 1 (c) – (f) show the change in the image upon laser excitation for several representative time delays [i.e. $I(t_j) - I(\text{off})$]. The data $I(t_j)$ are obtained by averaging 100 images with 100 single-pulse exposures per image. Initially, the areas near the zone-centers brighten at $t = 0$ ps (c) while the scattering increases for several hundred ps after excitation (d) and (e), before decreasing after a few ns (f), eventually returning to equilibrium.

While most of the increase in scattering occurs on the 100 ps timescale, Figures 1 (c) - (f) show subtle differences that suggest that thermal equilibrium has not yet been achieved. To emphasize these differences, in Fig. 1 (g) we plot $I(400 \text{ ps}) - I(100 \text{ ps})$ normalized by $I(\text{off})$. If the lattice were in thermal equilibrium, Fig. 1 (g) would be uniform (in the classical limit) and proportional to the relative difference in temperature $T(400 \text{ ps}) - T(100 \text{ ps})$. However, the nontrivial pattern shows areas where the relative scattering increases (bright) and areas where it decreases (dark) and suggests that a more complex nonthermal dynamics in the phonon population is taking place where some phonon modes deplete while others continue to populate even at 400 ps.

In order to understand which phonons contribute to the diffuse scattering images at

scattering vector \mathbf{Q} , we consider the intensity of one-phonon scattering¹⁶,

$$I_1(\mathbf{Q}) \propto \sum_j \frac{1}{\omega_j(\mathbf{q})} \left(n_j(\mathbf{q}) + \frac{1}{2} \right) |F_j(\mathbf{Q})|^2, \quad (1)$$

where $\omega_j(\mathbf{q})$ is the frequency of the phonon mode in branch j with reduced wavevector \mathbf{q} , $n_j(\mathbf{q})$ is its population and $F_j(\mathbf{Q})$ is

$$F_j(\mathbf{Q}) = \sum_s \frac{f_s}{\sqrt{m_s}} e^{-M_s(\mathbf{Q} \cdot \hat{\mathbf{e}}_{s,j,\mathbf{q}})} e^{-i\mathbf{K}_Q \cdot \mathbf{r}_s}. \quad (2)$$

In this expression, f_s , m_s , M_s are the atomic scattering factor, the mass, and the Debye-Waller factor¹⁷ of atom s at position \mathbf{r}_s , $\hat{\mathbf{e}}_{s,j,\mathbf{q}}$ is the phonon polarization vector, and \mathbf{K}_Q is the closest reciprocal lattice vector to \mathbf{Q} , i.e. $\mathbf{Q} = \mathbf{q} + \mathbf{K}_Q$. In Eq. (1) we omitted additional slowly varying factors from the polarization dependence of the scattering as well as geometrical factors¹⁶.

Eq. (1) gives a strong contribution from acoustic modes near the center of the Brillouin zone where their frequency goes to zero. These low-frequency phonons give rise to the four brightest diffuse spots in Fig. 1 (a). Directions in reciprocal space where the dispersion relation is soft appear in Fig. 1 (a) as bright lines connecting the near-zone-center spots. Furthermore, the quantity $F_j(\mathbf{Q})$ in Eq. (2) has the form of a structure factor modified by the dot product $(\mathbf{Q} \cdot \hat{\mathbf{e}}_{s,j,\mathbf{q}})$, which selects phonon modes polarized along the scattering vector. Finally, the eight small spots of a few pixels in diameter in Fig. 1 (a) [not present in the calculated image, Fig. 1 (b)] are crystal surface truncation rods and are well known from surface diffraction¹⁸.

Equations (1) and (2) can be used to compute the TDS if the phonon frequencies *and* eigenvectors are known. To gain insight on the different phonon contributions we implement a Born model of the lattice dynamics. For each vector \mathbf{Q} , we construct the dynamical matrix $\mathbf{D}(\mathbf{Q})$ using force constants up to six nearest neighbors. Details of the implementation of the model can be found in Refs.^{19,20}. The phonon polarization and frequencies in Eq. (1) and (2) are obtained from the eigenvalues and eigenvectors of $\mathbf{D}(\mathbf{Q})$. The 28 parameters that represent the real space covalent forces for InP and InSb were taken from Refs.²¹ and²² respectively. This model ignores the ionic component of the forces and thus does not reproduce the phonon dispersion with all detail, particularly it does not give a splitting of the LO and TO phonons at zone-center for the zinc-blende structure. However the insight gained is extremely valuable for understanding the static diffuse images particularly in separating

the contributions from transverse (TA) and longitudinal (LA) acoustic phonons. As we see in Fig. 1 (b), the calculation agrees well with the static measurements and reproduces the main features.

To help identify the phonons responsible for the nonequilibrium behavior, we performed singular value decomposition (SVD) of the time-resolved data, $I(t_j) - I(\text{off})$. The procedure is as follows. We write each difference frame $I(t_j) - I(\text{off})$ as a column vector \mathbf{x}_j and construct the matrix \mathbf{X} whose columns are the vectors \mathbf{x}_j . Thus, adjacent columns of \mathbf{X} correspond to consecutive frames in the time-delay series. The SVD states that $\mathbf{X} = \mathbf{U}\mathbf{S}\mathbf{V}^T$, where $\mathbf{S} = \text{diag}(s_i)$ is the diagonal matrix of singular values with $s_i \geq 0$, and \mathbf{U} and \mathbf{V} are orthogonal matrices whose columns, \mathbf{u}_j and \mathbf{v}_j , are the left and right singular vectors, respectively. The vectors \mathbf{u}_j represent time-independent “populations”, and form a complete orthonormal basis. The vectors \mathbf{v}_j contain the time-dependent information of each of the populations and also form an orthonormal basis. The singular values $\{s_i\}$ act as weight factors for these vectors and represent the amount of “signal” contained in each singular vector in the reconstructed data. This method has been applied successfully to a wide set of problems from small angle scattering²³ and the analysis of spectroscopic data²⁴ to time-resolved Laue diffraction of protein crystals²⁵. In Fig. 2 we summarize the results of the SVD analysis for both InP [(a) and (b)] and InSb [(c) and (d)]. The truncation rods were masked out to avoid artifacts from saturated pixels. Due to the larger lattice constant, the data for InSb were taken at 13 keV to match the same reciprocal space coverage on the detector as InP at 15 keV. On the left we show the lSV for the two most significant SV, while on the right we plot the corresponding rSV scaled by the corresponding SV. Singular values for which the rSV showed comparable amplitudes for $t < 0$ and $t > 0$ were considered comparable to the noise. Under this truncation criteria only the first two singular vectors shown in Fig. 2 are statistically significant. For both materials, much of the signal is contained in the first singular vector [Fig. 2 (a) and (c)], the time dependence of which consists of a sharp increase in the diffuse scattering that decays in few ns time scale (Fig. 2 (a) and (c) right panels). The image from this lSV resembles the equilibrium image, which suggests this lSV corresponds to lattice heating and diffusion that decays within a time-scale of few ns.

The second singular vectors however show a more complex behavior both in reciprocal space as well as in the time domain. In the case of InP, the lSV [Fig. 2 (b) (left)] shows sharp bright and dark areas indicating that parts of the image brighten while other areas

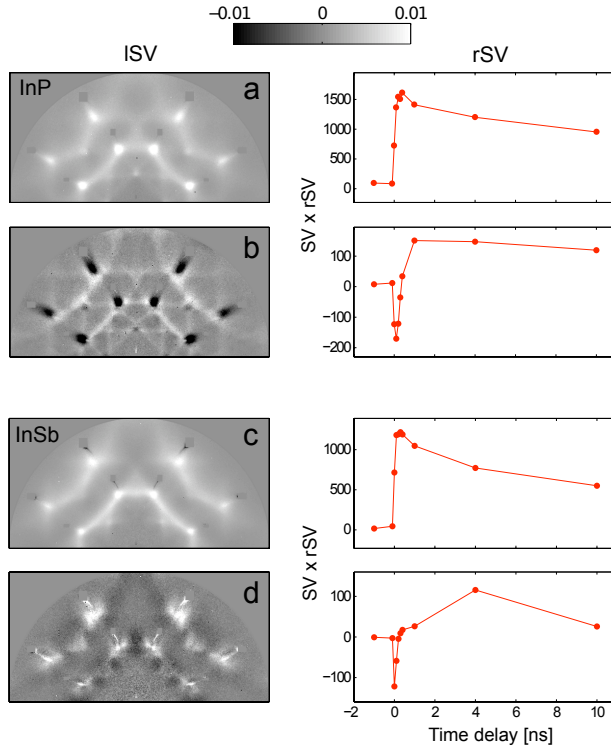


FIG. 2: Results of the singular value decomposition analysis of the time-resolved data. The procedure decomposes the data as a sum of individual images (ISV) (left) each with a corresponding time dependence (rSV) scaled by the corresponding SV (right). (a) and (b) correspond to the two most significant singular values for InP and (c) and (d) for InSb.

decrease their scattering. The fact that the rSV [Fig. 2 (b) (right)] increases only after $t \approx 400$ ps means that the corresponding pattern on the left continues increasing after the initial excitation. This is indicative of non-equilibrium phonon dynamics that lead to a delayed heating and cooling of different parts of the Brillouin-zone. A similar delayed behavior is observed in InSb as seen in Fig. 2 (d) (right), which shows a maximum increase at ~ 4 ns. We attribute this behavior to relaxation of non-equilibrium phonon populations.

Although the (equilibrium) TDS distributions for InP and InSb are similar, as well as the first singular vector in Fig. 2 (a) and (c), which reflects similarities in the phonon dispersion, the difference in the second ISV is quite remarkable and cannot be explained by differences in the equilibrium phonon dispersion alone. It is instructive to separate the contribution from different phonon branches to the diffuse scattering. Each phonon branch contributes

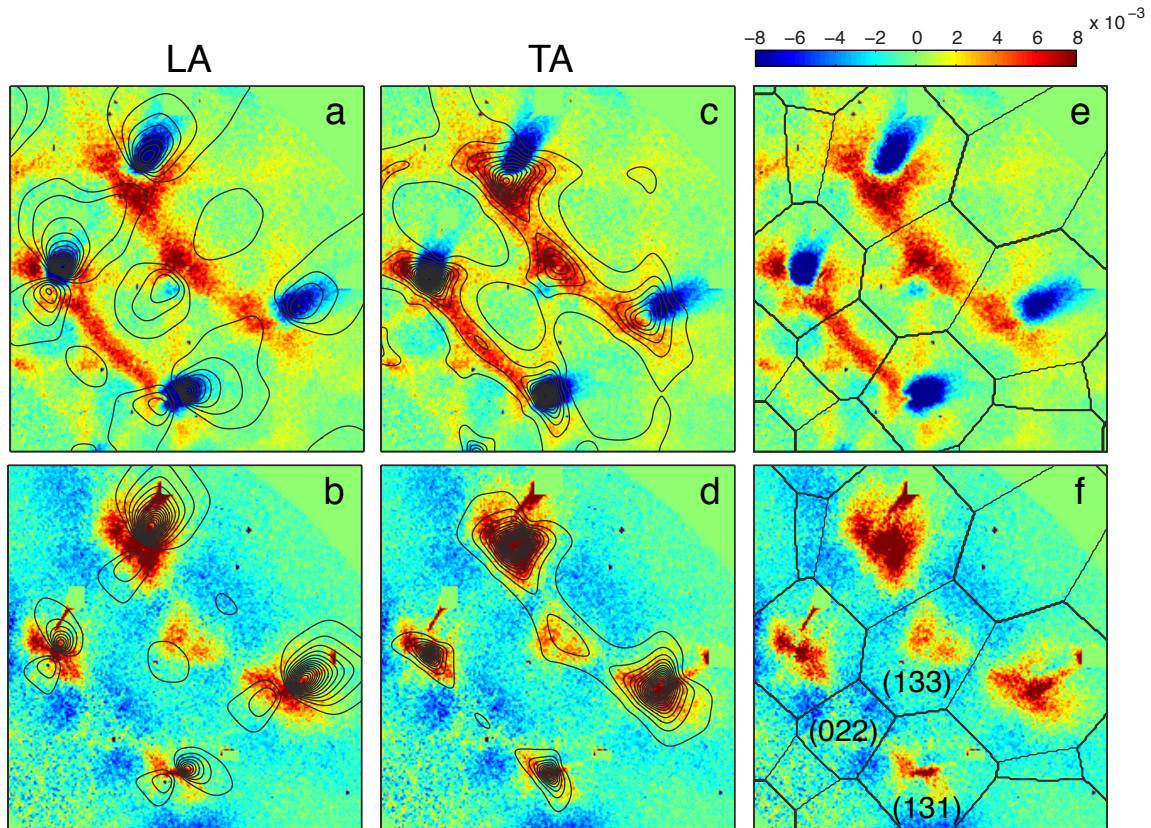


FIG. 3: Contribution to the TDS from TA and LA branches calculated using Eq. (1). The images are the second ISV in Fig. 2 (b) (top row) and Fig. 2 (d) (bottom row). The contours in (a) and (b) show the calculated contribution from LA phonons in InP and InSb, respectively. (c) and (d) show the contribution from TA phonons for InP and InSb, respectively. (e) and (f) show the Brillouin-zone boundaries for InP and InSb superimposed on the ISV. In (f) we show Miller indices for selected Brillouin-zones of InSb.

one term to Eq. (1), which we compute using the Born model described above. The top and bottom rows of Fig. 3 show a zoomed view of the second ISV in Fig. 2 (b) and (d), respectively. Superimposed, we show contour plots that represent the calculated contribution to Eq. (1) from the LA [(a) and (b)] and the TA [(c) and (d)] branches separately. As stated earlier, the largest contribution to the scattering comes from areas that are close to the center of the Brillouin-zone, where the contours lines are denser. This is further confirmed by superimposing the images with the corresponding Brillouin-zone boundaries as shown in (e) and (f).

From Fig. 3 (c) we see that for InP the areas with strong contribution from TA phonons

appear bright in the ISV, while areas with more contribution from the LA branch [Fig. 3 (a)] appear dark. This ISV has the time-dependence shown in the right panel of Fig. 2 (b), which means that even at time-delays $t > 400$ ps TA phonons are still populating while the LA branch population decreases. In InSb the situation is different. The LA branch shows no appreciable decrease in scattering above the noise level [Fig. 3 (b)], while the TA branches populate delayed [Fig. 3 (d)]. In Fig. 3 (f) we indicate the Miller indices of selected Brillouin-zones for InSb at 13 keV. Note that at this energy the number and size of Brillouin zones covered by the detector in InSb is similar to InP at 15 keV. We can assign the InP TA phonons in Fig. 3 (c) to modes with \mathbf{q} approximately along the high-symmetry $\langle 111 \rangle$ and $\langle 010 \rangle$ directions. InSb on the other hand shows a less directional scattering from the TA branches, indicating that the population is distributed more isotropically within the Brillouin-zone. We attribute this difference to the large gap between the optical and acoustic modes in InP, which leads to less available phonon decay channels².

IV. CONCLUSIONS

We have shown that time-resolved non-thermal x-ray diffuse scattering yields heretofore inaccessible information of the non-equilibrium dynamics of solids under ultrafast excitation. InP and InSb show complex non-equilibrium redistributions of the scattered intensity throughout the Brillouin-zone that are clearly separated by singular value decomposition. This non-equilibrium lattice persists up to several hundred ps. This behavior is interpreted using a Born model which reveals that TA phonons populate several hundred ps after initial laser excitation and, in the case of InP, is very directional and appears concomitant with a decrease in the scattering by LA phonons. In the current study, we are limited to dynamics that occur on more than 100 ps time-scale due to the x-ray pulse duration. We note that measurements of the initial emission of hot phonons by the photoexcited carriers and their subsequent anharmonic decay will become possible with new x-ray sources such as the Linac Coherent Light Source at SLAC. As these new sources of ultra-bright femtosecond x-ray pulses come online, x-ray diffuse scattering becomes a promising approach to explore the ultrafast dynamics of solids under laser excitation at the femtosecond time-scale.

V. ACKNOWLEDGEMENTS

We acknowledge S. Ghimire for experimental assistance and H. Dosch and T. C. Chiang for fruitful discussions. This research is supported through the PULSE Institute at the SLAC National Accelerator Laboratory by the U.S. Department of Energy, Office of Basic Energy Sciences. V. H. V. was supported by the Air Force Office of Science Research under contract FA9550-08-1-0340 from the Multidisciplinary University Research Initiative Program. Use of the Advanced Photon Source was supported by the U.S. Department of Energy, Basic Energy Sciences, Office of Science, under Contract No. DE-AC02-06CH11357. Use of the BioCARS Sector 14 was supported by the National Institutes of Health, National Center for Research Resources, under grant number RR007707. The time-resolved set-up at Sector 14 was funded in part through a collaboration with Philip Anfinrud (NIH/NIDDK).

* mtrigo@slac.stanford.edu

† currently at Los Alamos National Laboratory

- ¹ Jing Chen, J. B. Khurgin, and R. Merlin, *Appl. Phys. Lett.* **80**, 2901 (2002).
- ² A. Debernardi, *Phys. Rev. B* **57**, 12847 (1998).
- ³ R. James, *Optical Principles of the Diffraction of X-Rays* (G. Bell, London, 1954).
- ⁴ B. E. Warren, *X-Ray Diffraction* (Dover, New York, 1969).
- ⁵ D. B. McWhan, P. Hu, M. A. Chin, and V. Narayanamurti, *Phys. Rev. B* **26**, 4774 (1982).
- ⁶ L. D. Chapman, S. M. Hsieh, and R. Colella, *Phys. Rev. B* **30**, 1094 (1984).
- ⁷ S. D. LeRoux, R. Colella, and R. Bray, *Phys. Rev. Lett.* **35**, 230 (1975).
- ⁸ D. A. Reis and A. M. Lindenberg, in *Light Scattering in Solids IX, Topics in Applied Physics*, edited by M. Cardona and R. Merlin (Springer, 2007), vol. 108, pp. 371–422.
- ⁹ M. Trigo and D. Reis, *MRS Bulletin* **35** (2010).
- ¹⁰ R. E. Joynson, *Phys. Rev.* **94**, 851 (1954).
- ¹¹ E. H. Jacobsen, *Phys. Rev.* **97**, 654 (1955).
- ¹² H. Cole, *Journal of Applied Physics* **24**, 482 (1953).
- ¹³ H. Cole and B. E. Warren, *Journal of Applied Physics* **23**, 335 (1952).
- ¹⁴ B. N. Brockhouse and A. T. Stewart, *Phys. Rev.* **100**, 756 (1955).

- ¹⁵ M. Holt, Z. Wu, Hawoong Hong, P. Zschack, P. Jemian, J. Tischler, Haydn Chen, and T.-C. Chiang, *Phys. Rev. Lett.* **83**, 3317 (1999).
- ¹⁶ Ruqing Xu and Tai C. Chiang, *Z. Kristallogr.* **220**, 1009 (2005).
- ¹⁷ J. F. Vetelino, S. P. Gaur, and S. S. Mitra, *Phys. Rev. B* **5**, 2360 (1972).
- ¹⁸ I. K. Robinson, *Phys. Rev. B* **33**, 3830 (1986).
- ¹⁹ Helen M. J. Smith, *Phil. Trans. Roy. Soc. Lond.* **241**, 105 (1948).
- ²⁰ Frank Herman, *J. Phys. Chem. Solids* **8**, 405 (1959).
- ²¹ H.-M. Kagaya and T. Soma, *phys. stat. sol. (b)* **121**, K113 (1984).
- ²² T. Soma and H. Matsuo Kagaya, *phys. stat. sol. (b)* **118**, 245 (1983).
- ²³ Shigeru Okamoto and Shinichi Sakurai, *Journal of Applied Crystallography* **36**, 982 (2003).
- ²⁴ Eric R. Henry, *Biophysics Journal* **72**, 652 (1997).
- ²⁵ Marius Schmidt, Sudarshan Rajagopal, Zhong Ren, and K. Moffat, *Biophysics Journal* **84**, 2112 (2002).